Ray-Based Evaluation of Dual-Polarized MIMO in (Ultra-)Dense Millimeter-Wave Urban Deployments

Dmitrii Solomitckii*, Vitaly Petrov*, Hosein Nikopour†, Mustafa Akdeniz†, Oner Orhan†,
Nageen Himayat†, Shilpa Talwar†, Sergey Andreev*, and Yevgeni Koucheryavy*
*Tampere University of Technology, Tampere, Finland
†Intel Labs, Santa Clara, CA, USA
Email: firstname.lastname@tut.fi, firstname.lastname@intel.com

***Abstract*—Dense deployments of millimeter-wave (mmWave) base stations (BSs) are being considered as the most feasible solution to meet the steadily growing data rate demands of mobile users. Accordingly, the achievable performance gains of mmWave-based dense networks in real deployments have to be studied carefully, since mmWave radio technology features specific transceiver, antenna, and propagation properties. In this paper, we contribute an accurate performance evaluation of single- versus dual-polarized MIMO systems operating over the mmWave channel in typical urban scenarios as well as address the impact of device- and network-centric parameters on the performance gains enabled by MIMO in dense to ultra-dense BS deployments. This study relies on our in-house ray-based modeler and takes into account the key mmWave system effects, such as multi-path propagation, utilization of dual-polarized antennas, and characteristic interference models. Our results show that the benefit of using mmWave-MIMO grows with increasing BS density, thus encouraging a further study of this technology especially for (ultra-)dense setups. We also demonstrate that non-coherent non-polarized diffuse scattering component may reduce the capacity gain of dual-polarized vs. single-polarized MIMO.**

I. Introduction

The New Radio (NR) technology operating over the millimeter-wave (mmWave) spectrum enables the next generation of wireless communication systems aiming to provide improved data rate, latency, and energy-efficiency to mobile users [1]. While the standardization process of the key NR features as part of the fifth-generation (5G) mobile networks is almost complete [2], and the vendors are testing their early implementations [3], the question of what would be the quantitative gains of several advanced mmWave features in real-world deployments and thus is it worth implementing them, remains open [4], [5].

One of the emerging features of the mmWave radio as compared to microwave systems is its inherent ability to operate with compact large-scale antenna arrays [6]. The use of such arrays enables higher directionality of mmWave transmissions, dynamic beam steering and beamforming [7], [8], as well as allows to effectively construct multiple-input multiple-output (MIMO) systems and hence increase the capacity by transmitting multiple data streams in parallel [9].

While the capacity gain of MIMO utilization over mmWave is notable [10], [11], the actual improvement may vary drastically subject to both the environment- and the implementation-specific parameters [12], [13]. Broadly, the existing investigations on MIMO systems capacity can be divided into two groups: (i) general analytical evaluations and (ii) site-specific simulation studies. The authors of the first class of works aim to develop an analytical framework for a generalized (abstract) deployment, so that their model may be applicable to a wide range of scenarios. On the contrary, the second group of papers is dedicated to in-depth analysis of a particular deployment, such that the applicability of the results is exchanged for their accuracy.

There are numerous visible works in the first category. The authors of [14] investigate the system capacity for a group of interfering users that employ single-user detection and multiple transmit/receive antennas over flat Rayleigh-fading channels. Another work in [15] proposes a simple prediction model of MIMO systems capacity by using vertically polarized and dual-polarized antennas. Finally, the study in [16] addresses the potential benefits of dual-polarized arrays in multi-antenna wireless systems. There are more studies in the first group, but all of them introduce certain simplifying assumptions for the sake of modeling tractability, which affects the accuracy of the final results and, consequently, becomes the motivation for the second category of contributions.

The site-specific research typically incorporates detailed ray-based simulations of a given scenario by taking into account realistic antenna gains, site-specific channel gains, and other relevant physical features [17]. For instance, the authors of [18] investigate the channel characteristics for a compact 2x2 MIMO dipole antenna array with decoupling by using ray-tracing simulations. The study presented in [19] addresses the capacity of a 4x4 MIMO system operating at 2.55 GHz and 24 GHz bands through site-specific simulations as well. Finally, the work in [20] reports on the channel behavior with mmWave massive MIMO at 26 GHz.

However, the dense and, especially, ultra-dense deployments of base stations (BSs) in urban scenarios introduce certain additional effects that have to be carefully taken into account in the MIMO studies. The first one is related to inter-cell interference that is typically disregarded in the technical literature, which mainly focuses on the point-to-point mmWave communications [21]. Another one is the effect of realistic beam patterns at both the BS and the user equipment (UE) sides, which is different from idealistic models (e.g., a cone) assumed in many works on the topic [22]. Finally, the utilization of

practical dual-polarized antennas has additional implications on the system behavior. To the best of our knowledge, there has been no study that addresses the capacity gains of MIMO in (ultra-)dense mmWave deployments by carefully accounting for all the aforementioned important effects.

Aiming to bridge this gap, this paper presents an in-depth study of a dense mmWave network with MIMO capabilities. We apply our in-house ray-based simulation framework [23], which is extended to accurately model the effects of (i) inter-cell interference, (ii) dual-polarized antennas, and (iii) practical beam patterns from the codebooks, as well as all the crucial mmWave propagation phenomena, such as reflection, diffraction, and diffuse scattering within the environment. We thus study the capacity gains of mmWave MIMO in realistic urban deployments by quantifying the effects of beamwidth and inter-site distance (ISD). We believe that our evaluation methodology and obtained numerical results may be further employed for the applicability assessment of mmWave MIMO systems in certain practical scenarios.

The rest of this paper is organized as follows. In Section II, the scenario of interest and the deployments under consideration are summarized. Section III outlines the developed evaluation methodology with a focus on the mmWave- and MIMO-specific features. The key numerical results are reported and explained in Section IV, while Section V discusses the important physical effects behind the presented results. The conclusions are drawn in the last section.

II. Considered Deployment

Here, we utilize the Manhattan grid scenario that represents a typical urban area. It has a grid of square buildings (see Fig. 1), 6,500 outdoor UEs (dots in Fig. 1), and a number of mmWave BSs (max 131 items for the highest density). The latter are arranged as a grid with variable ISD between the adjacent nodes 90, 180, and 360 m, while the UE-grid has a constant step of 5 m. It should be noted that depending on the density of the mmWave BSs, the numbers of UEs in the line-of-sight (LoS) and the non-LoS (NLoS) conditions vary. The following proportions of the LoS and NLoS UEs have been considered across the deployment: (i) ultra-dense, $ISD = 90$ m, $UE_{LoS} = 100\%$, $UE_{NLoS} = 0\%$; (ii) dense, $ISD = 180$ m, $UE_{LoS} = 67\%$, $UE_{NLoS} = 23\%$; and (iii) low-dense/sparse, $ISD = 360$ m, $UE_{LoS} = 17\%$, $UE_{NLoS} = 83\%$.

The mmWave carrier frequency utilized in all of our simulations is 28 GHz, which is envisioned for the initial 5G mmWave cellular deployments [24]. In the subsequent study, we primarily focus on the downlink transmissions. The remaining parameters of our deployment of interest are summarized in Table I.

III. Developed Evaluation Methodology

This section summarizes our evaluation methodology. Subsection III-A introduces our methodology at-a-glance, subsection III-B explains the details of how the antenna polarization effects are taken into account, while the implementation of the diffuse scattering model is explained in subsection III-C, and the procedure of MIMO capacity evaluation is outlined in subsection III-D.

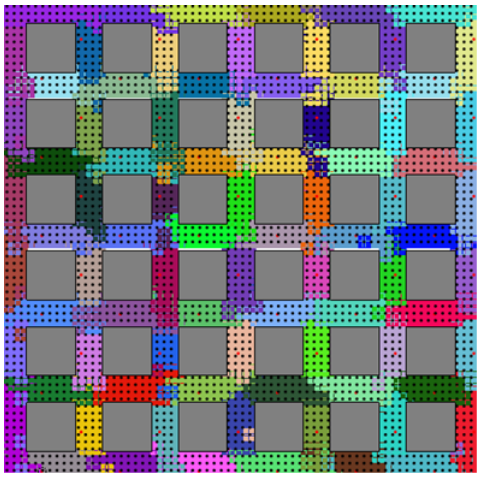

Fig. 1. Urban mmWave deployment of interest. Gray-colored squares represent buildings and black dots are UEs. Each color demonstrates a certain group of UEs belonging to a single mmWave BS.

TABLE I
Considered Scenario Parameters

Parameter	Value
Total square, m	800 x 800
Propagation area, m	600 x 600
Building, m	60 x 60 x 100
Road width, m	20
Wall width, m	0.3
Wall material	concrete
Selected ISDs, m	90, 180, 360
Selected HPBWs, °	12, 30, 50
Carrier frequency, GHz	28
Bandwidth, GHz	0.5
Noise figure, dB	7

A. Methodology-at-a-Glance

Our evaluation methodology utilized in this paper comprises two stages: (i) deterministic ray-based simulation and (ii) refining procedure. The first stage is carried out by our in-house ray-based modeler, which was calibrated against the recent mmWave numerology in various scenarios [23], [25]. The tool is used to model all of the possible connections between every UE-BS pair and characterize the mmWave radio channel between them. The output of the first stage is the channel impulse response (CIR) between each Tx antenna at the mmWave BS and Rx antenna at the UE:

$$h(\tau,\theta,\gamma) = \sum_{n=1}^{N} a_n exp(j\phi_n)\delta(\tau-\tau_n)\delta(\phi^{Rx}-\phi_n^{Rx}) \\ \delta(\theta^{Rx}-\theta_n^{Rx})\delta(\phi^{Tx}-\phi_n^{Tx})\delta(\theta^{Tx}-\theta_n^{Tx}), \quad (1)$$

where a_n is the amplitude of n^{th} multipath component arriving at a certain Tx antenna of a particular UE from the direction having azimuth and elevation components (angle of arrival, AoA) as follows $[\phi^{Rx},\theta^{Rx}]$. At the same time, $[\phi^{Tx},\theta^{Tx}]$ describes the departure direction (angle of departure, AoD)

of n^{th} multipath component from the antenna of a particular mmWave BS. The output data is stored in a sorted database.

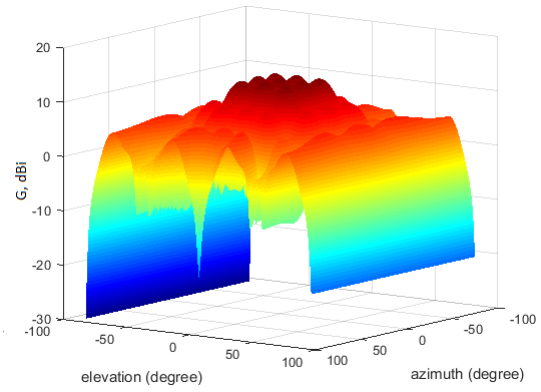

Fig. 2. Typical codebook with HPBW = 50° oriented along ϕ = 0° and θ = 0°. The main lobe consists of multiple smaller beams due to large HPBW.

Once all of the CIRs are obtained, the refining stage begins by applying a channel access abstraction that models a round-robin algorithm together with the corresponding antenna radiation patterns. The overall evaluation process can be briefly summarized as follows:

1) Each UE is associated with a serving BS based on the SNR maximization criterion.
2) Each of the BSs randomizes the order of UEs associated to it, so that the scheduling interval for the UE does not depend on its initial number. This step is needed to accurately model the inter-cell interference.
3) Simulations are run in a time-driven fashion. During each of the scheduling intervals, the BS selects a UE from its list. For the selected UE, the serving BS defines the best AoD and AoA according to the SNR multi-paths.
4) Both the BS and the UE search for the most beneficial antenna pattern (w.r.t. the SNR maximization criterion) from their codebooks and thus align the main lobes of their beams according to the estimated AoA and AoD values. Accordingly, the "best" beam configuration between each of the UE and the associated BS is established and the mmWave channel between them can now be evaluated.
5) The tool sequentially calculates the capacity for each BS-UE link by carefully considering the impact of inter-cell interference.
6) Return to step 2) to randomize the interference.
7) After a given number of rounds, the data for the current sample is stored, while the deployment becomes randomized and the procedure reiterates. Steps 2)–6) are repeated and the intermediate statistics are collected for each of them.
8) For the sake of higher accuracy in the mean output results, the intermediate values for each of the samples are averaged over 100 replications.

In this study, the practical codebooks were used that represent realistic antenna radiation patterns at mmWave frequencies. The employed codebooks cover all of the possible azimuthal and elevation directions. The number of utilized codebooks per a simulation run depends on their HPBW (169 codebooks for HPBW = 13° and 9 for HPBW = 50°). An example codebook with HPBW = 50° oriented at $\phi = 0°$ and $\theta = 0°$ is illustrated in Fig. 2.

We believe that the proposed approach offers appropriate balance between accuracy and flexibility. Its inherent advantage is that the ray-based geometry between the BS and the UE does not have to be recalculated at every step, as it is typically done in the state-of-the-art solutions. Instead, our tool models a scenario with omnidirectional antenna radiation patterns only once and then produces the final results by adjusting the data at the output of the omnidirectional modeling according to the selected antenna radiation pattern: certain rays become stronger or weaker depending on the AoA, AoD, and the antenna radiation pattern. However, our numerical results remain in-line with those contributed by the past studies in [26], [27].

B. Considering Polarization

To model the MIMO channel between the UE(s) and the mmWave BS(s), all of them were equipped with 8x8 antenna arrays in case of single polarization and with 16x16 arrays in case of dual polarization (slanted antennas). The latter option was simulated as two collocated 8x8 antenna arrays with the relative orthogonal polarizations of +/-45°. Hence, based on electromagnetic theory, such slanted orientation might be resolved as a combination of both the vertical and the horizontal components of electrical field radiated by the antenna:

$$\mathbf{E_{tot}} = \hat{\mathbf{e}_{\|}} E^{\|} + \hat{\mathbf{e}_{\perp}} E^{\perp}, \tag{2}$$

where $\hat{e_{\|}}$ and $\hat{e_{\perp}}$ are the basis. This means that a signal radiated from such a slanted antenna carries both polarization components by default and thus each of them suffers from intermediate interaction with the surrounding objects. It is represented in our methodology via dyadic reflection and diffraction coefficients. It was also assumed that a single Tx antenna at the BS side communicates with each Rx antenna at the UE side. Therefore, when receiving a signal for which polarization differs by 90° from the polarization of the receiving antenna, the received power level will be negligible.

C. Diffuse Scattering Effects

With respect to the existing studies, an additional Lambertian model of diffuse scattering on reflection was added to our proposed methodology. This model was included after several preliminary simulations in order to strengthen the potential output results (will be discussed in detail in Section IV). Following the said model, a signal reflecting from a surface with certain effective roughness produces the coherent (specular) and incoherent (diffuse scattering) components being radiated by the surface. Specifically, specular amplitude is negatively related to the diffuse scattering components through the coefficient of roughness. Accordingly, the total signal

strength of the UE's Rx is a combination of the specular and the diffuse scattering paths: $E_{tot} = E_{spec} + E_s$. Here, the magnitude of diffuse scattering electrical field is represented by the following equation [28]:

$$|E_s|^2 = |E_{s0}|^2 \cdot cos(\theta_s) = \frac{dS \cdot S^2 \cdot cos(\theta_i) \cdot cos(\theta_s)}{\pi r_i^2 \cdot r_s^2}. \quad (3)$$

In (3), $|E_{s0}|$ is the amplitude of a radiated signal, θ_s and θ_i are the angles of scattered and incident fields, r_i is the distance from the Tx to the area of scattering, and r_s is the distance from the area of scattering to the Rx. Each of the building walls is divided into multiple tiles (scattering sources) with the linear size of dS. Finally, S is a coefficient that defines the amount of scattered field with respect to the incident field and demonstrates the diffuse scattering capability of a certain surface, such that $S = \frac{E_s}{E_i}$. The value of S may be calculated analytically from the reflection and roughness coefficients, but we here adopt specific practical values of 0.1, 0.3, and 0.6 from [29], [30]. We additionally assume that a diffuse scattered signal is incoherent, which means that each scattered ray carries a randomly polarized signal [31] i.e., the polarization vector may be oriented in any direction.

D. Capacity of mmWave MIMO System

In order to post-process the calculated intermediate results and estimate the capacity of the mmWave MIMO system, the following canonical approach has been utilized:

$$C = \log_2 \det(\mathbf{I} + \mathbf{P_i^{-1}} \mathbf{P_{rx}}), \quad (4)$$

where the power at Rx might be represented as a combination of the co- and cross-polarized power of a multipath signal. The latter is given by:

$$\mathbf{P_{rx}} = \frac{1}{N} \begin{pmatrix} P_{vv}^{Rx} & P_{vh}^{Rx} \\ P_{hv}^{Rx} & P_{hh}^{Rx} \cdot \end{pmatrix}. \quad (5)$$

Further, to simplify the numerical calculations, the matrix responsible for the co-channel interference has been rewritten as follows:

$$\mathbf{P_i} = \begin{pmatrix} NL + P_{vv}^i & NL \\ NL & NL + P_{hh}^i \end{pmatrix}, \quad (6)$$

where NL is the noise level set to 80 dBm, which corresponds to 0.5 GHz of bandwidth, while I_{vv} I_{hh} are the interfering power from the mmWave BSs to $+45°$ and $-45°$.

In (4), the component $\mathbf{P_i^{-1}} \mathbf{P_{rx}}$ represents the ideal SINR, which may reach an impractical value of over 35 dB. To incorporate the realistic limits imposed by the practical mmWave modulation and coding schemes (MCSs) [32], we add the error vector magnitude (EVM) to the estimated signal, which maximum value is set to 27 dB. Generally, this parameter is a measure of error in the constellation of a modulated signal, which actually determines the maximum SINR that might be reached at the Rx side in the case of no additional impairments to the Tx signal [33]. Adjusting the SINR with the help of the EVM has been implemented by using the following equation:

$$\frac{1}{SINR_{EVM}} = \frac{1}{SINR} + \frac{1}{EVM}. \quad (7)$$

An additional cap was further applied to the maximum achievable value of the spectral efficiency as 4.8 bit/s/Hz, which corresponds to 64QAM with the coding rate of 4/5. The minimum sensitivity level for the outage conditions was also introduced ($SINR < -6$ dB in our case), which defines the minimum supported SINR along the list of the utilized MCSs. We offer the numerical results produced by our evaluation methodology in the following section.

IV. Numerical Results

First, we present the cumulative distribution function (CDF) of the UE spectral efficiency by taking into account different HPBWs (13°, 30°, and 50°) and ISDs (180 m and 360 m). The output results for the single- and dual-polarized MIMO spectral efficiency are displayed in Fig. 3. These plots confirm that in the low-dense (ISD = 360 m) and, especially, dense (ISD = 180 m) regime, higher gains of the antenna radiation pattern lead to better spectral efficiency. Specifically, in Fig 3(a) (ISD = 180 m), the spectral efficiency is within the range of 2.0–4.8 bit/s/Hz, while Fig. 3(c) (ISD = 360 m) demonstrates the range of 0–2.1 bit/s/Hz, correspondingly. For dual-polarized MIMO, the respective values are: 3.9–9.6 bit/s/Hz for ISD = 180 m, see Fig. 3(b), and 0–3.9 bit/s/Hz for ISD = 360 m, see Fig. 3(d). Another interesting observation from Fig. 3 is that ISD = 180 m guarantees that all of the UEs have their spectral efficiency of over 0, while 50–60% of the UEs are in outage (spectral efficiency is zero) with ISD = 360 m. Here, with large ISD the system operates primarily in the noise-limited regime, while the contribution of interference becomes of secondary importance.

We further study the capacity gain provided by a dual-polarized system vs. a single-polarized counterpart. To this aim, the ratios of the two average capacities are calculated as Capacity Gain = C_{dual}/C_{single}, while the output is collected in Fig. 4. Understanding the results in Fig. 4, we conclude that the capacity of a dual-polarized MIMO system decreases with the increase in the ISD as well as the impact of the non-polarized diffuse scattering (coefficient S). When diffuse scattering is small ($S = 10\%$), the slope of the dashed line is negligible and none of the HPBWs provide with any notable advantage in terms of capacity. In particular, the capacity gain at ISD = 90 m is about 1.98 (98% improvement), whereas the one at ISD = 360 m is 1.95. Further increase in S to 0.3 leads to a non-uniform decrease in the gain down to 1.95 at ISD = 90 m and 1.84 at ISD = 360 m, respectively. The most significant decrease in the capacity gain is observed at $S = 0.6$, when the ISD is equal to 360 m (only 1.74). Based on the technical literature, further growth of S is impractical for urban deployments [31].

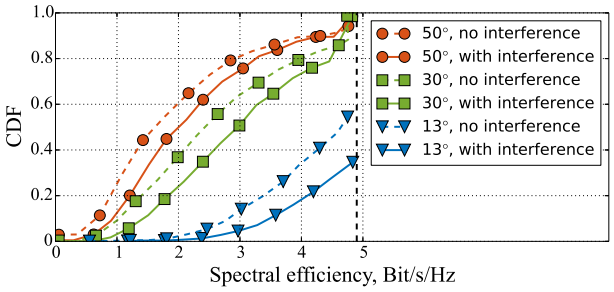

(a) ISD = 180 m, single stream

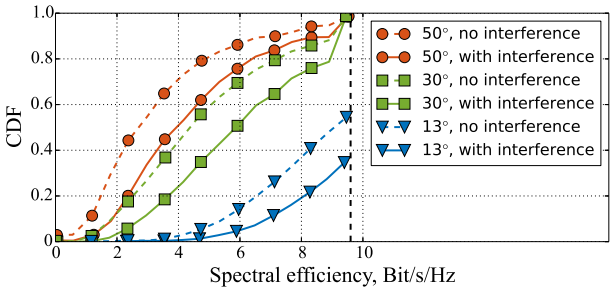

(b) ISD = 180 m, dual stream

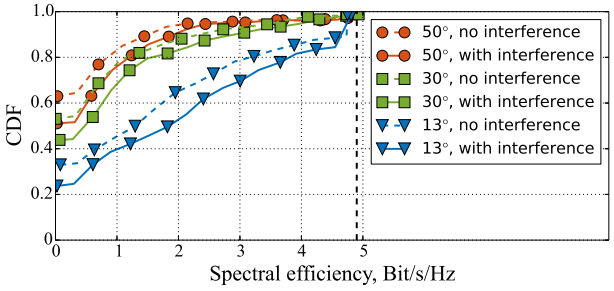

(c) ISD = 360 m, single stream

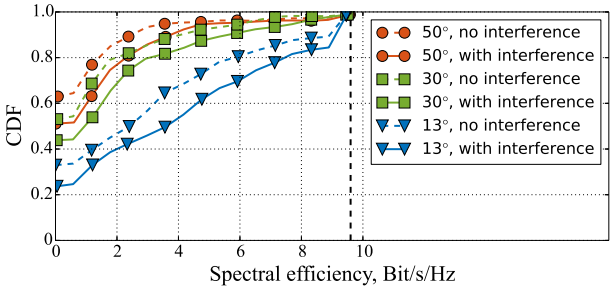

(d) ISD = 360 m, dual stream

Fig. 3. Spectral efficiency for single- and dual-polarized mmWave MIMO system at S = 0.1, different ISDs and HPBWs.

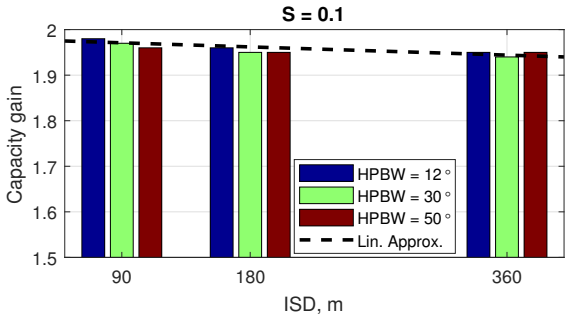

(a)

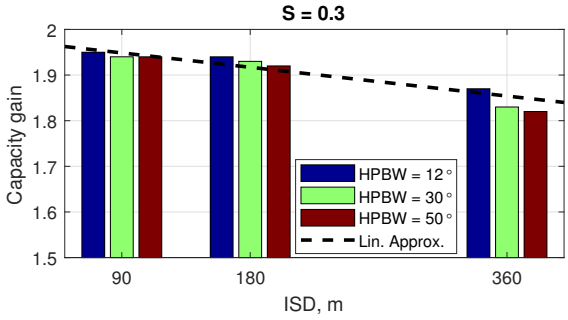

(b)

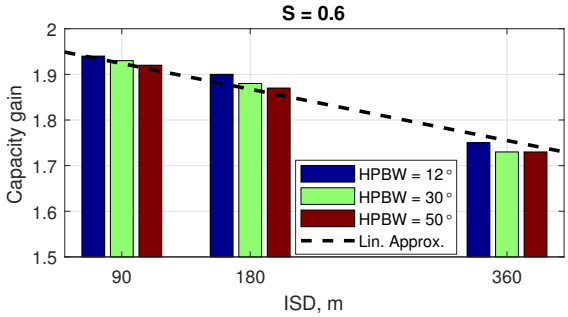

(c)

Fig. 4. Capacity gain for single-polarized MIMO channel vs. dual-polarized MIMO-channel as a function of ISD, HPBW, and diffuse scattering coefficient. Capacity gain reduces significantly with distance and the amount of scattered field. Also, some decrease in capacity occurs with growing HPBW.

V. Discussion

A polarized MIMO channel with two orthogonal branches provides a higher number of uncorrelated communication channels (channel matrix rank is 2), which could potentially double the channel capacity. However, based on our simulation results, the idealistic value of 2 has never been achieved subject to practical losses due to signal attenuation, scattering, and inter-cell interference. Particularly, a gradual decrease of capacity occurs with the growing distance, HPBW, and, especially, the environment property *S*. Below, we briefly explain and interpret these observations.

Theoretically, an arbitrarily polarized signal (having both polarization components) that impinges on a free-oriented surface may change its polarization after a reflection. It happens because the reflection coefficients (often named the Fresnel coefficients) are different for the two polarization types, see Fig. 5. Hence, the horizontal component attenuates faster with respect to the vertical component after each reflection. Subsequently, two signals emitted by any mmWave BS with orthogonal polarization and suffering from intermediate interaction with the objects can no longer be considered in isolation with respect to each other at the UE side, since the polarization angle cannot be 90°. This effect is known as *depolarization* and leads to an imbalance of the matrix in (5) by increasing the

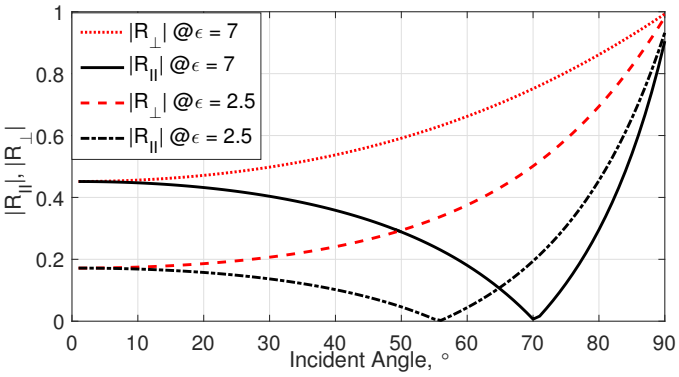

Fig. 5. Reflection coefficient R for horizontal (black) and vertical (red) polarization. Higher dielectric permittivity ε leads to larger reflection coefficient and thus greater reflected power.

non-diagonal received power components and thus decreasing the total capacity.

On the other hand, despite the fact that more reflections make depolarization higher, the amplitude of the signal is steadily dropping. The degradation rate depends on the angle of incidence and the dielectric permittivity of a surface. Fig. 6 demonstrates a situation where the dielectric permittivity of surrounding walls is $\varepsilon = 7$ (concrete at mmWave). Accordingly, it can be observed that the original signal (normalized for simplification) sent by a single slanted antenna (+45°) changes its amplitude and orientation of the polarization vector toward vertical direction after each step of reflection. Therefore, the highest probability of depolarization may occur when the incident angle α is large and the material is not transparent for transmission. The second criterion is based on the propagation principle where transmission and reflection are negatively related to each other through the dielectric permittivity, ε: higher reflectivity is connected to smaller transmission capability.

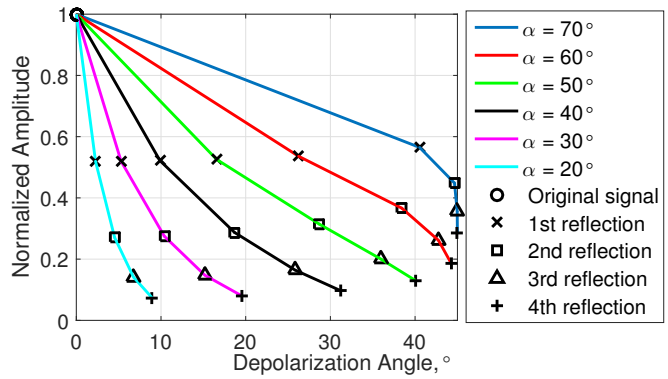

Fig. 6. Signal impinging on a surface experiences a depolarization effect by changing its polarization by a certain angle. Greater angle of incidence α leads to more significant depolarization.

Another criterion of wide incident angle is when the UE and the BS are located far from each other (case BS2-UE1 in Fig. 7) or close to a building (case BS1-UE2 in Fig. 7).

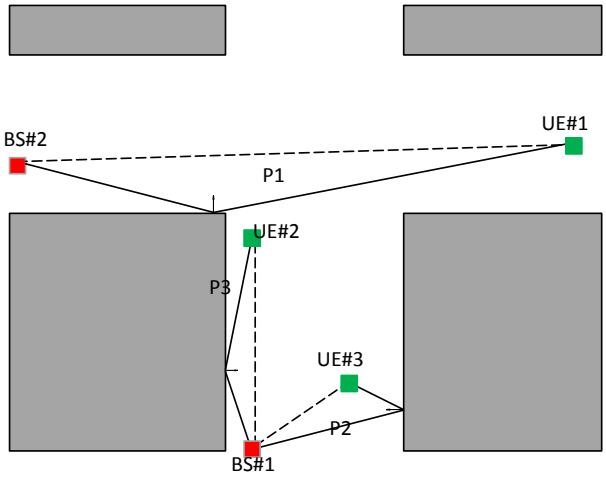

Fig. 7. Favorable (BS1-UE2 and BS2-UE1) and unfavorable (BS1-UE3) conditions for emergence of cross-polarization losses.

Due to the fact that the core of our methodology exploits a specular reflection model from the conditionally idealized surface (without irregularities, roughness, detailization, etc.), the impact of cross-polarization components may be underestimated. Moreover, the average cross-polarization ratio (XPR) is on the order of 30 dB, which is rather high [34], [35].

To improve on this situation, a model for the first-order diffuse scattering from surface irregularities was introduced to our methodology. It operates as an additional amplification of the cross-polarized received power. However, the functionality of this model is limited and thus the impact on MIMO capacity is reduced. Primarily, it is connected with significant attenuation and the contribution of power. Consequently, it should also be mentioned that in the presence of a LoS-path (or another strong path), the effect of depolarization is negligible. Therefore, even in diffuse scattering rich deployments, the capacity of a dual-polarized MIMO system with small ISDs practically does not change. However, with the increasing ISD and subsequently growing number of NLoS UEs, the influence of depolarizing paths improves, which leads to a decrease in capacity. In such conditions, small capacity drops as HPBW widens are associated with larger diffusing areas on walls, which also somewhat degrade the capacity.

VI. Conclusions

Dense and ultra-dense mmWave networks are envisioned to soon become an integral part of 5G and beyond-5G wireless systems. While the incorporation of mmWave technology brings notable gains in the network capacity, research currently investigates if these benefits can be increased further by the use of advanced radio techniques. In this paper, a detailed analysis of the mmWave MIMO system in a realistic deployment has been conducted. It was shown that the gain of using the dual-polarized mmWave array vs. the single-polarized option varies in the range of 1.7–2 with the BS density and the directivity of the preferred antenna radiation pattern. It was also demonstrated that the negative effect of interference at

higher densities of BSs is well mitigated by the fact that the overwhelming majority of the UEs are in the LoS conditions with respect to the associated BS. Accordingly, the impact of the mmWave MIMO is the greatest for the highest considered density of the BSs, thus advocating for the use of MIMO systems in dense and, especially, ultra-dense urban mmWave deployments.

ACKNOWLEDGMENT

This work was supported by Intel Corporation, by the Academy of Finland (projects WiFiUS and PRISMA), and by the project TAKE-5: The 5th Evolution Take of Wireless Communication Networks, funded by Tekes. V. Petrov acknowledges the support of HPY Research Foundation funded by Elisa.

REFERENCES

[1] S. Y. Lien, S. L. Shieh, Y. Huang, B. Su, Y. L. Hsu, and H. Y. Wei, "5G New Radio: Waveform, Frame structure, Multiple Access, and Initial Access," *IEEE Communications Magazine*, vol. 55, no. 6, pp. 64–71, 2017.

[2] A. A. Zaidi, R. Baldemair, M. Andersson, S. Faxer, V. Moles-Cases, and Z. Wang, "Designing for the future: The 5G NR physical layer," *Ericsson Technology Review*, pp. 1–13, June 2017.

[3] W. Hong, K. H. Baek, Y. Lee, Y. Kim, and S. T. Ko, "Study and prototyping of practically large-scale mmWave antenna systems for 5G cellular devices," *IEEE Communications Magazine*, vol. 52, pp. 63–69, September 2014.

[4] M. Xiao *et al.*, "Millimeter wave communications for future mobile networks [Editorial]," *IEEE Journal on Selected Areas in Communications*, vol. 35, pp. 1909–1935, September 2017.

[5] V. Petrov, D. Solomitckii, A. Samuylov, M. A. Lema, M. Gapeyenko, D. Moltchanov, S. Andreev, V. Naumov, K. Samouylov, M. Dohler, and Y. Koucheryavy, "Dynamic multi-connectivity performance in ultra-dense urban mmWave deployments," *IEEE Journal on Selected Areas in Communications*, vol. 35, pp. 2038–2055, September 2017.

[6] H. K. Pan, B. D. Horine, M. Ruberto, and S. Ravid, "Mm-wave phased array antenna and system integration on semi-flex packaging," in *Proc. of IEEE International Symposium on Antennas and Propagation (IEEE APSURSI)*, pp. 2059–2062, July 2011.

[7] S. Jayaprakasam, X. Ma, J. W. Choi, and S. Kim, "Robust beam-tracking for mmwave mobile communications," *IEEE Communications Letters*, vol. 21, pp. 2654–2657, December 2017.

[8] V. Petrov, D. Moltchanov, and Y. Koucheryavy, "Applicability assessment of terahertz information showers for next-generation wireless networks," in *Proc. of IEEE International Conference on Communications (ICC)*, pp. 1–7, May 2016.

[9] S. Sun, T. S. Rappaport, R. W. Heath, A. Nix, and S. Rangan, "MIMO for millimeter-wave wireless communications: Beamforming, spatial multiplexing, or both?," *IEEE Communications Magazine*, vol. 52, pp. 110–121, December 2014.

[10] J. Mo and R. W. Heath, "High SNR capacity of millimeter wave MIMO systems with one-bit quantization," in *Proc. of Information Theory and Applications Workshop (ITA)*, pp. 1–5, February 2014.

[11] S. A. Hoseini, M. Ding, and M. Hassan, "A new look at MIMO capacity in the millimeter wave," in *Proc. of IEEE Global Communications Conference (GLOBECOM)*, December 2017.

[12] M. K. Samimi, S. Sun, and T. S. Rappaport, "MIMO channel modeling and capacity analysis for 5G millimeter-wave wireless systems," in *Proc. of 10th European Conference on Antennas and Propagation (EuCAP)*, pp. 1–5, April 2016.

[13] J. C. Shen, J. Zhang, and K. B. Letaief, "Downlink user capacity of massive MIMO under pilot contamination," *IEEE Transactions on Wireless Communications*, vol. 14, pp. 3183–3193, June 2015.

[14] R. S. Blum, "MIMO capacity with interference," *IEEE Journal on Selected Areas in Communications*, vol. 21, pp. 793–801, June 2003.

[15] V. Eiceg, H. Sampath, and S. Catreux-Erceg, "Dual-polarization versus single-polarization MIMO channel measurement results and modeling," *IEEE Transactions on Wireless Communications*, vol. 5, pp. 28–33, January 2006.

[16] C. Oestges, B. Clerckx, M. Guillaud, and M. Debbah, "Dual-polarized wireless communications: from propagation models to system performance evaluation," *IEEE Trans. Wireless Commun.,*, pp. 4019–4031, Oct. 2008.

[17] C. Wang, H. Papadopoulos, K. Kitao, and T. Imai, "Ray-tracing based performance evaluation of 5G mmWave massive MIMO in hotspots," in *Proc. of International Symposium on Antennas and Propagation (ISAP)*, pp. 608–609, October 2016.

[18] M. M. Taygur, W. K., and E. T. E., "Ray tracing based channel analysis involving compact MIMO antenna arrays with decoupling networks," *Proc. of the 20th International ITG Workshop on Smart Antennas (WSA 2016)*, March 2016.

[19] J. W. Wallace, W. Ahmad, Y. Yang, R. Mehmood, and M. A. Jensen, "A comparison of indoor MIMO measurements and ray-tracing at 24 and 2.55 GHz," *IEEE Transactions on Antennas and Propagation*, vol. 65, pp. 6656–6668, December 2017.

[20] B. Ai, K. Guan, R. He, J. Li, G. Li, D. He, Z. Zhong, and K. M. S. Huq, "On indoor millimeter wave massive MIMO channels: Measurement and simulation," *IEEE Journal on Selected Areas in Communications*, vol. 35, pp. 1678–1690, July 2017.

[21] D. Solomitckii, V. Petrov, H. Nikopour, M. Akdeniz, O. Orhan, N. Himayat, S. Talwar, S. Andreev, and Y. Koucheryavy, "Detailed interference analysis in dense mmWave systems employing dual-polarized antennas," in *Proc. of IEEE Globecom Workshops (GC Wkshps)*, pp. 1–7, December 2017.

[22] V. Petrov, M. Komarov, D. Moltchanov, J. M. Jornet, and Y. Koucheryavy, "Interference analysis of EHF / THF communications systems with blocking and directional antennas," in *Proc. of IEEE Global Communications Conference (GLOBECOM)*, pp. 1–7, December 2016.

[23] D. Solomitckii, Q. C. Li, T. Balercia, C. R. C. M. da Silva, S. Talwar, S. Andreev, and Y. Koucheryavy, "Characterizing the impact of diffuse scattering in urban millimeter-wave deployments," *IEEE Wireless Communications Letters*, vol. 5, pp. 432–435, August 2016.

[24] M. R. Akdeniz, Y. Liu, M. K. Samimi, S. Sun, S. Rangan, T. S. Rappaport, and E. Erkip, "Millimeter wave channel modeling and cellular capacity evaluation," *IEEE Journal on Selected Areas in Communications*, vol. 32, pp. 1164–1179, June 2014.

[25] D. Solomitckii, M. Gapeyenko, S. S. Szyszkowicz, S. Andreev, H. Yanikomeroglu, and Y. Koucheryavy, "Toward massive ray-based simulations of mmWave small cells on open urban maps," *IEEE Antennas and Wireless Propagation Letters*, vol. 16, pp. 1435–1438, December 2017.

[26] 3GPP, "Channel model for frequency spectrum above 6 GHz (Release 14)," 3GPP TR 38.900 V2.0.0, 2016.

[27] "METIS channel models," Tech. Rep. ICT-317669-METIS/D1.4, METIS, February 2015.

[28] V. Degli-Esposti, D. Guiducci, A. de'Marsi, P. Azzi, and F. Fuschini, "An advanced field prediction model including diffuse scattering," *IEEE Transactions on Antennas and Propagation*, vol. 52, pp. 1717–1728, July 2004.

[29] V. Degli-Esposti and H. L. Bertoni, "Evaluation of the role of diffuse scattering in urban microcellular propagation," *Proc. IEEE Vehicular Technology Conference (IEEE VTC)*, p. 1922, September 1999.

[30] J. Pascual-Garcia, M. T. Martinez-Ingles, J. M. Molina-Garcia-Pardo, J. V. Rodrguez, and V. Degli-Esposti, "Experimental parameterization of a diffuse scattering model at 60 GHz," in *Proc. of IEEE-APS Topical Conference on Antennas and Propagation in Wireless Communications (APWC)*, pp. 734–737, September 2015.

[31] V. Degli-Esposti, F. Fuschini, E. M. Vitucci, and G. Falciasecca, "Measurement and modelling of scattering from buildings," *IEEE Transactions on Antennas and Propagation*, vol. 55, no. 1, pp. 143–153, 2007.

[32] R. Ford, M. Zhang, S. Dutta, M. Mezzavilla, S. Rangan, and M. Zorzi, "A framework for end-to-end evaluation of 5G mmWave cellular networks in ns-3," in *Proc. of the Workshop on Ns-3*, ACM, 2016.

[33] E. Dahlman, S. Parkvall, and J. Skold, *4G, LTE-advanced Pro and the Road to 5G*. Academic Press, 2016.

[34] K. Haneda, J. Zhang, L. Tan, G. Liu, Y. Zheng, H. Asplund, J. Li, Y. Wang, D. Steer, C. Li, *et al.*, "5G 3GPP-like channel models for outdoor urban microcellular and macrocellular environments," in *Proc. of IEEE Vehicular Technology Conference (IEEE VTC)*, IEEE, 2016.

[35] C. Gustafson, D. Bolin, and F. Tufvesson, "Modeling the polarimetric mm-wave propagation channel using censored measurements," in *Proc. of IEEE Global Communications Conference (IEEE GLOBECOM)*, IEEE, 2016.